Nanoscale Advances

ROYAL SOCIETY OF CHEMISTRY

PAPER

View Article Online
View Journal | View Issue

Cite this: *Nanoscale Adv.*, 2025, **7**, 886

In situ synthesis of gold nanoparticles embedded in a magnetic nanocomposite of glucosamine/alginate for enhancing recyclable catalysis performance of nitrophenol reduction†

Le-Kim-Thuy Nguyen,[ab] Manh-Huy Do,[ab] Phuoc-Dat Duong,[ab] Thi-My-Duyen Tran,[a] Thi-Quynh-Nhu Ngo,[a] Xuan -Thom Nguyen,[a] Van-Dung Le,[ab] Cao-Hien Nguyen,[c] Radek Fajgar [d] and Thanh-Danh Nguyen *[ab]

Received 25th November 2024
Accepted 16th December 2024

DOI: 10.1039/d4na00979g

rsc.li/nanoscale-advances

In this study, we introduce an *in situ* synthesis technique for incorporating gold nanoparticles (AuNPs) into a magnetic nanocomposite made of glucosamine and alginate (GluN/Alg) *via* ionotropic gelation. GluN acted as a reducing agent for gold ions, leading to the formation of AuNPs which embedded in the nanocomposite Fe_3O_4@GluN/Alg. Analytical techniques confirmed the crystallite structure of the nanocomposite AuNPs/Fe_3O_4@GluN/Alg, which had an average size of 30–40 nm. This nanocomposite demonstrated high catalytic efficiency in reducing 2-, 3-, and 4-nitrophenols, exhibiting rapid kinetics with pseudo-first order rate constants between 1.16×10^{-3} s^{-1} and 2.29×10^{-3} s^{-1}. The reduction rates and recyclability for nitrophenols followed the order: 4-nitrophenol > 2-nitrophenol ~ 3-nitrophenol. These results indicate that the nanocomposite holds significant promise for customized applications in environment and medicine, positioning it as a highly versatile material.

1. Introduction

Gold nanoparticles (AuNPs) have garnered significant attention due to their diverse applications in biomedicine,[1,2] sensing,[3,4] and catalysis.[5,6] An emerging trend in nanotechnology is the synthesis of AuNPs using eco-friendly sources such as microbial and plant extracts.[7,8] These nanoparticles are particularly effective as catalysts for removing environmental contaminants from aqueous solutions. Key factors influencing the catalytic activity of nanoparticles include their morphology and the capping agents used, as these elements impact both the stability and the surface-to-volume ratio, thus enhancing the availability of active sites.[9,10]

Despite the benefits, conventional synthesized AuNPs presents challenges, including high costs and limited stability. To address these issues, researchers have explored embedding AuNPs into various carrier materials. For example, magnetic nanoparticles are highly regarded in catalysis due to their ease of recyclability.[11,12] Additionally, polymers are commonly used to support AuNPs in various applications.[13,14] Among these, polysaccharides stand out for their ability to stabilize AuNPs effectively, thanks to the hydroxy groups in their sugar molecules, which form strong associations with the nanoparticles.[15,16] Liu *et al.* demonstrated the effective application of AuNPs/Fe_3O_4-chitosan composites in the recyclable reduction of methyl orange.[17] AuNPs were synthesized by reducing Au^{3+} ions in alkaline conditions[17] or with $NaBH_4$.[18] Kang *et al.* successfully developed an AuNPs/Fe_3O_4@cellulose nanocomposite through a two-step process, using sodium citrate as a reducing agent for Au^{3+} ions.[19] These studies highlight the efficiency of polysaccharides as carrier agents for AuNPs/Fe_3O_4 nanoparticles. However, the synthesis of AuNPs typically involves a two-step process that requires additional reducing agents.

Recent advancements have seen the synthesis of AuNPs integrated into alginate, which have demonstrated remarkable efficacy in the recyclable catalysis for reduction of 4-nitrophenol [20] and the degradation of toxic dyes.[21] Recently, Ghorbani-Vaghei *et al.*[22] successfully synthesized Fe_3O_4@Alg-AuNPs nanocomposites through a two-step process: first, by capping Fe_3O_4@Alg with Au^{3+} ions, followed by reducing them to Au nanoparticles (AuNPs) using sodium citrate. These

[a]*Institute of Chemical Technology, Vietnam Academy of Science and Technology, 1A TL29 Street, District 12, Ho Chi Minh City 700000, Vietnam. E-mail: ntdanh@ict.vast.vn; danh5463bd@yahoo.com*

[b]*Graduate University of Science and Technology, Vietnam Academy of Science and Technology, 18 Hoang Quoc Viet, Cau Giay, Hanoi 11000, Vietnam*

[c]*Department of Chemical Technology, Ho Chi Minh City University of Industry and Trade, Ho Chi Minh City 700000, Vietnam*

[d]*Institute of Chemical Process Fundamentals of the AS CR Prague, Czech Republic*

† Electronic supplementary information (ESI) available: Physical parameters calculated from XRD patterns, XP spectroscopy, UV-vis spectra for reduction of nitrophenols without catalysts and kinetic data. See DOI: https://doi.org/10.1039/d4na00979g

nanocomposites demonstrated good catalytic activity in the reduction of 4-nitrophenol, with the reaction mechanism following the Langmuir–Hinshelwood model. In this mechanism, borohydride ions adsorb onto the catalyst's surface and transfer hydride ions to the AuNPs, while the Fe_3O_4 component acts as a recyclable agent. This innovative approach underscores the potential of these nanocomposites for sustainable and efficient environmental remediation. However, the fabrication process, involving a complex reduction step, is challenged by the high solubility of sodium alginate, which may lead to catalyst loss in aqueous environments.

Our previous research has demonstrated that metallic nanoparticles can be seamlessly incorporated into polysaccharides through an *in situ* reduction process, which eliminates the need for additional chemicals.[23,24] Recently, the ionotropic gelation mechanism has been used to create nanocomposites with polysaccharides like alginate and chitosan.[25,26] This method involves loading metallic ions onto the nanocomposite and subsequently reducing them to form nanoparticles. Using polysaccharides alongside reducing agents in this technique enhances cost efficiency and minimizes impurities or toxic byproducts. However, there has been no reported *in situ* synthesis and application of AuNPs embedded in magnetic polysaccharide nanoparticles. In this study, we present a straightforward method for synthesizing AuNPs loaded into a nanocomposite of Fe_3O_4 and glucosamine/alginate (GluN/Alg) without any additives. The resulting AuNPs/Fe_3O_4@GluN/Alg nanocomposite was thoroughly characterized physicochemically and tested for its catalytic efficiency in reducing nitrophenols.

2. Materials and methods

2.1. Materials

Chemicals including tetrachloroauric acid ($HAuCl_4$), calcium acetate monohydrate ($(CH_3COO)_2Ca\cdot H_2O$, code 447860010), sodium alginate ($C_6H_7O_6Na$, 177775000), D-glucosamine·HCl (GluN, 98%, 119901000), 2-nitrophenol (2-NP, 99%), 3-nitrophenol (3-NP, 99%), 4-nitrophenol (4-NP, 99%) were purchased from Acros Co. (Belgium). Fe_3O_4 NPs powder (97% trace metals basis, 1002834758) was purchased from Sigma-Aldrich. All experiments used the deionized water thoroughly.

2.2. Synthesis of nanocomposite AuNPs/Fe_3O_4@GluN/Alg

The GluN/Alg nanogel was synthesized using a modified ionotropic gelation method as previously described.[27] The gel was prepared with a mass ratio of GluN to Alg (1 : 4, w/w). To create Ca-Alg gelispheres, 20 mL of sodium alginate solution (7 mg mL^{-1}) was mixed with 7.2 mL of calcium acetate solution (6.5 mg mL^{-1}). Subsequently, 14.7 mL of the GluN solution (1.6 mg mL^{-1}) was added dropwise to the gelisphere suspension. The mixture was stirred for 60 minutes to form the GluN/Alg nanogel, which was then washed multiple times with water and purified by centrifugation.[23,28]

A suspension of $HAuCl_4$ and Fe_3O_4 in varying ratios was stirred at 400 rpm for 120 minutes at room temperature, then added to the GluN/Alg nanogel. This mixture was stirred and heated to form the AuNPs/Fe_3O_4@GluN/Alg nanocomposite. In all experiments, the Fe_3O_4 to nanogel ratio was maintained at 1 : 1 (w/w). The synthesis process was monitored using UV-vis spectroscopy. The nanocomposites were purified through magnetic separation, washed with water (3 × 10 mL), and vacuum dried at 60 °C for 90 minutes to obtain the pure nanocomposite. The solid nanocomposites were used to characterize XPS, XRD, TGA and DSC.

2.3. Characterisation of nanocomposite AuNPs/Fe_3O_4@GluN/Alg

The UV-vis spectra were recorded using a JASCO V-630 spectrophotometer, covering a wavelength range of 300–800 nm.

The suspension of nanocomposites in water was dropped to surface of films before measurement of transmission electron microscopy (TEM) and field emission scanning electron microscopy (FESEM). TEM and FE-SEM were measured by a Hitachi H810, and JSM7401F (Japan), respectively. The size distribution was calculated with ImageJ software.

Zeta potential measurements was carried out using nanocomposite gel suspensions, collected after washing and dissolving in water. The measurement was taken at 25 °C with an applied voltage of 3.3 V.

Magnetic properties were examined using a MicroSense VSM 9.13 L vibrating sample magnetometer (USA).

Powder X-ray diffraction (XRD) patterns were obtained with a Shimadzu 6100 X-ray diffractometer (Japan). The crystalline size was calculated using the Debye–Scherrer equation, $D = 0.9\lambda/\beta\cos\theta$, where D is the mean size of the gold crystals, β is the full width at half maximum (FWHM) in radians, λ is the wavelength of the CuKα X-ray radiation (0.1540 nm), and θ is the Bragg diffraction angle in radians.

Thermogravimetric analysis (TGA) and differential thermal analysis (DTA) were conducted using a LabSys evo S60/58988 Thermoanalyzer (Setaram, France). These analyses were performed over a temperature range of 30 °C to 800 °C, with a heating rate of 10 °C per minute in an air atmosphere.

The chemical component analysis and surface stoichiometry of the nanocomposites were performed *via* X-ray photoelectron spectroscopy (XPS, ESCA 3400, Kratos, U.K.) in the analysis using a polychromatic MgK_α X-ray source (1254.6 eV, 120 W). Survey (step 0.2 eV) and high resolution (step 0.05 eV) spectra of the samples were measured. Peak analysis was performed using CasaXPS using a Shirley-type background and symmetric Gauss–Lorentzian lines shapes GL(30) applied in convolution. The spectra were calibrated using C 1s (284.8 eV).

2.4. Reduction of nitrophenols

The catalytic efficiency of the AuNPs/Fe_3O_4@GluN/Alg nanocomposites was assessed by reducing nitrophenols, specifically 2-NiP, 3-NiP, and 4-NiP. The reaction was carried out with a ratio $NaBH_4$/NiPs/catalyst = 504/23/1 (w/w/w). The mixture of $NaBH_4$ (0.5 mL, 0.2 M) and NiPs (2.5 mL, 0.5 mM) was reacted at room temperature. All reactions were conducted in a 1.0 cm path length cuvette. Subsequently, the nanocomposite catalyst

(6 mg) was introduced into the mixture. The catalytic activity and reaction kinetics were monitored using UV-vis spectroscopy, measuring absorbance changes at 414 nm for 2-NiP, 390 nm for 3-NiP, and 400 nm for 4-NiP at two-minute intervals.

A rapid decline in the absorbance of the nitrophenols was observed at their respective wavelengths upon addition of the nanocomposites, indicating effective catalytic reduction. The reaction kinetics were analyzed using a pseudo-first-order model to determine the catalytic performance of the nanocomposites.

Within the Langmuir–Hinshelwood model, it is assumed that the diffusion and adsorption of reactants onto the catalyst surface occur rapidly, while the reduction of NiPs is the slow, rate-determining step. Consequently, the reaction rate (r_t) is proportional to the apparent rate constant (k_{app}), the surface area (S), and the surface coverage (θ) of the catalyst with reagents, as described by the following equation:

$$r_t = -\frac{dC_{NiP}}{dt} = kS\theta_{NiP}\theta_{BH_4^-} = k_{app}C_{NiP} \quad (1)$$

The surface coverage of nitrophenols (θ_{NiP}) and borohydride ions ($\theta_{BH_4^-}$) are given by:

$$\theta_{NiP} = \frac{(k_{NiP}C_{NiP})^a}{1 + (k_{NiP}C_{NiP})^a + (k_{BH_4^-}C_{BH_4^-})^b} \quad (2)$$

$$\theta_{BH_4^-} = \frac{(k_{BH_4^-}C_{BH_4^-})^b}{1 + (k_{NiP}C_{NiP})^a + (k_{BH_4^-}C_{BH_4^-})^b} \quad (3)$$

where C_{NiP} and $C_{BH_4^-}$ are the concentrations of NiPs and BH_4^- ions, respectively. The exponents a and b are related to the equilibrium between adsorption and desorption processes, indicating the heterogeneity of the sorbents. In the classical Langmuir isotherm model, both parameters are equal to 1. Therefore, eqn (1) can be simplified to:

$$-\frac{dC_{NiP}}{dt} = \frac{kSk_{NiP}C_{NiP}k_{BH_4^-}C_{BH_4^-}}{(1 + k_{NiP}C_{NiP} + k_{BH_4^-}C_{BH_4^-})^2} = k_{app}C_{NiP} \quad (4)$$

From this, the apparent rate constant k_{app} can be expressed as:

$$k_{app} = \frac{kSk_{NiP}k_{BH_4^-}C_{BH_4^-}}{(1 + k_{NiP}C_{NiP} + k_{BH_4^-}C_{BH_4^-})^2} \quad (5)$$

Integrating eqn (1) gives:

$$\ln\left(\frac{C_{NiP0}}{C_{NiP}}\right) = k_{app}t \quad (6)$$

A plot of $\ln(C_{NiP}0/C_{NiP})$ or $\ln(A_0/A_t)$ *versus* reaction time yields a straight line, from which the rate constant k_{app} (s^{-1}) can be determined from the slope.

For investigation on reusability of the AuNPs/Fe_3O_4@GluN/Alg nanocomposites, the catalyst was retrieved using an external magnetic field, thoroughly washed with ethanol and distilled water, and then vacuum-dried at 60 °C for 60 minutes. To evaluate the recycling capability, the recovered catalyst was used in the reduction of nitrophenols (NiPs) for five consecutive runs under the same reaction conditions.

To assess the metallic ion content in the nanocomposite AuNPs/Fe_3O_4@GluN/Alg-15% before and after five reuse cycles for reduction of 4-NiP, 3.0 mg of the nanocomposite was dissolved in 5 mL of concentrated hydrochloric acid (35.5%) with gentle heating. The concentrations of iron and gold were then analyzed using the ICP-OES technique on an ICP-OES 5800 Agilent system.

3. Results and discussion

3.1. Synthesis of nanocomposite AuNPs/Fe_3O_4@GluN/Alg

The synthesis strategy for AuNPs/Fe_3O_4@GluN/Alg nanocomposites is depicted in Fig. 1. The GluN/Alg nanogel was prepared *via* an ionic gelation mechanism, as described in previous studies.[23,24] In this process, GluN provided a negative charge, disrupting cross-links between Ca^{2+} ions and COO^-

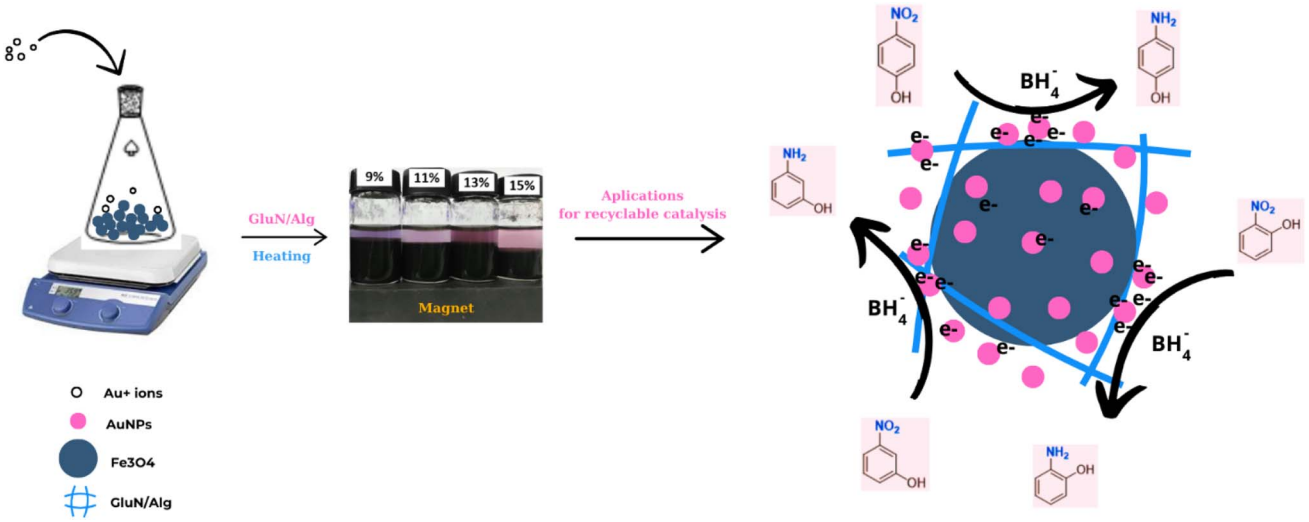

Fig. 1 Schematic route for synthesis and applications of nanocomposite AuNPs/Fe_3O_4@GluN/Alg.

groups in the Ca/Alginate gelispheres, resulting in the formation of dispersible GluN/Alg nanoparticles. Upon addition of Au^{3+}/Fe_3O_4 to the GluN/Alg, an *in situ* reduction occurred during a heating process, forming the AuNPs/Fe_3O_4@GluN/Alg nanocomposite without additional reductants. The formation of the nanocomposite was confirmed by a change in the color of the colloidal solution as shown in Fig. 1. Various reaction conditions were explored to optimize the synthesis of the AuNPs/Fe_3O_4@GluN/Alg nanocomposites. These nanocomposites were then characterized using a range of physicochemical analytical techniques and tested for their catalytic efficacy in reducing nitrophenols.

For the formation of AuNPs, the synthesis parameters influencing the reduction process, including reaction time and gold ion feed ratios, were investigated using UV-vis spectroscopy over a wavelength range of 450–750 nm. Variations in absorbance and λ_{max} values at the SPR band (around 500 nm) provide crucial insights into the size, morphology, and yield of the nanoparticles. The absorption data indicated that the formation of AuNPs/Fe_3O_4@GluN/Alg nanocomposites was highly dependent on all examined parameters, as evidenced by the differing trends observed (Fig. 2). The time-dependent reduction of gold ions was studied over a period of 0 to 100 minutes. It was generally found that the reduction process did not occur at reaction times shorter than 20 minutes, as indicated by the absence of the SPR band for AuNPs in the UV-vis spectra. The absorbance values of the SPR band increased significantly after 20 minutes of reaction and stabilized around 80 minutes, both in terms of absorbance and wavelength (Fig. 2A and B). This confirms that the concentration and morphology of AuNPs in the synthesized colloidal solutions undergo significant changes after 80 minutes of heating.

To investigate the effect of gold ions, the reduction process was carried out using various concentrations of Au^{3+} ions ranging from 1 to 15% (w/w) relative to Fe_3O_4 NPs. Absorption spectroscopy revealed that the SPR band was not clearly visible at feeding gold ion concentrations below 9% (w/w). The reduction efficiency increased with gold ion concentrations from 9 to 15% (w/w), as evidenced by the rise in absorbance values. Additionally, the observed decrease in wavelengths with higher feeding gold ion concentrations indicated a significant impact on the morphology of the nanocomposites. Consequently, nanocomposites synthesized with feeding gold ion concentrations of 9, 11, 13, and 15% would be further examined to explore their physicochemical properties and catalytic applications.

3.2. Characterizations of AuNPs/Fe_3O_4@GA/Alg

The stability of the nanocomposites in colloidal solutions was assessed through zeta potential measurements at room temperature, as shown in Fig. 3A. The zeta potential values for AuNPs/Fe_3O_4@GluN/Alg at 0%, 9%, 11%, 13%, and 15% were −44.8 mV, −46.5 mV, −37.6 mV, and −28.8 mV, respectively. These values were slightly lower than that of the nanocomposite

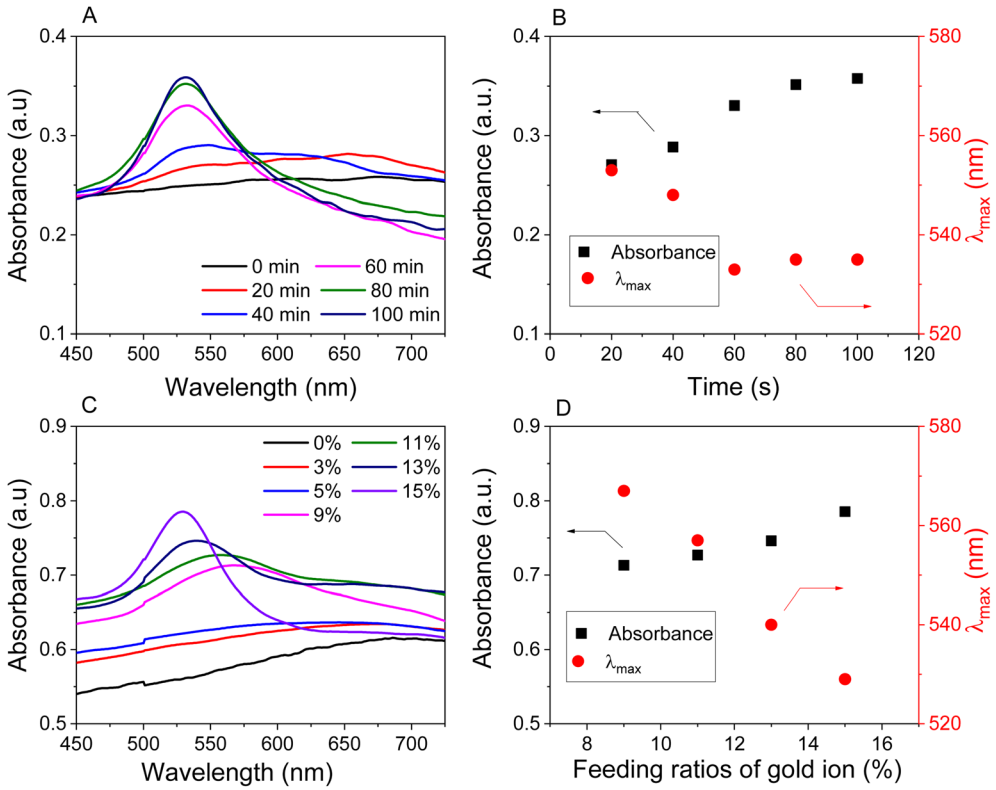

Fig. 2 UV-vis spectra (left) and plots of absorbance and wavelength (right) as functions of reaction conditions: reaction time for the sample with a feeding gold ion ratio of 15% (A and B), and various feeding ratios of gold ion to nanocomposite (w/w) (C and D).

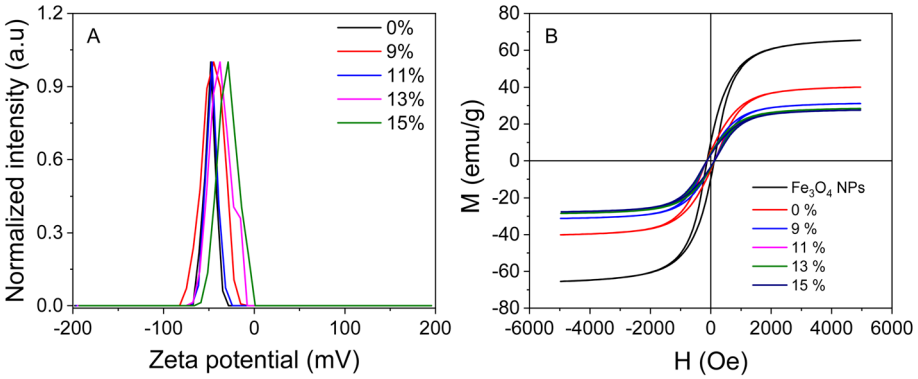

Fig. 3 (A) Zeta potential and (B) VSM curves for gel Fe_3O_4, and various feeding ratios of gold ions in Fe_3O_4@GluN/Alg gel.

without AuNPs (−47.8 mV). The reduction in zeta potential indicates that the presence of AuNPs decreased the negative charge of the nanocomposites, leading to reduced stability. Nevertheless, the zeta potentials of AuNPs/Fe_3O_4@GluN/Alg were still sufficient to maintain stability in the colloidal solution.

The magnetic properties of the AuNPs/Fe_3O_4@GluN/Alg nanocomposites were determined using VSM (Fig. 3B). The magnetization curves for all samples displayed a symmetrical hysteresis loop. The saturation magnetizations (M_s) of AuNPs/Fe_3O_4@GluN/Alg nanocomposites with 0%, 9%, 11%, 13%, and

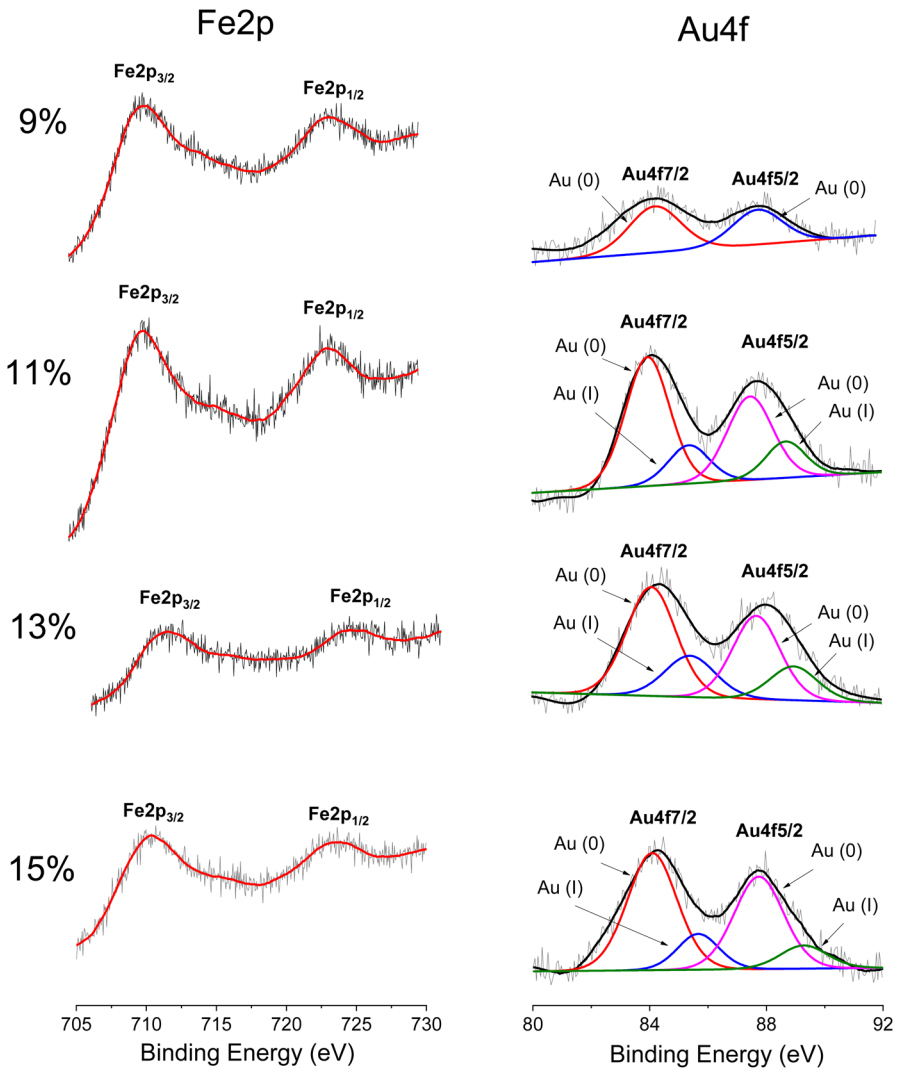

Fig. 4 High resolution XP spectra of Fe 2p and Au 4f elements in nanocomposite AuNPs/Fe_3O_4@GluN/Alg with various content of gold ions.

15% gold ion concentrations were 40.1, 31.1, 28.2, 28.4, and 27.5 emu g^{-1}, respectively. These values were significantly lower than that of Fe_3O_4 NPs (65.4 emu g^{-1}), due to the presence of nonmagnetic components such as GluN, Alg, and AuNPs. Despite this reduction, the saturation magnetization values were sufficiently high to allow easy separation of the nanocomposites using an external magnetic field, making them suitable for recyclable catalysis applications. The low coercivity (H_C) values of 118 Oe indicate that these materials exhibit superparamagnetic characteristics.[29]

The surface chemical composition of AuNPs/Fe_3O_4@GluN/Alg nanocomposites with varying gold content was analyzed using XPS spectroscopy. The survey spectra consistently showed characteristic peaks for Ca, Cl, Na, Fe, O, C, and Au. As depicted in Fig. S2,† the C 1s spectra of the nanocomposites reveal three contributions at 283.5 eV, 284.8 eV, and 286.4 eV, corresponding to carbidic species, sp^3 C–C, C–H, and C–O/C–O–C bonds typically found in polysaccharides.[30] Fig. 4 illustrates the Fe 2p spectra with broad peaks centered at 710.7 eV and 723.2 eV, indicative of Fe $2p_{3/2}$ and Fe $2p_{1/2}$ in Fe_3O_4, respectively.[28] The absence of a shakeup satellite peak around 719 eV, a marker for Fe_2O_3, further confirms the presence of Fe_3O_4 rather than Fe_2O_3.[31] The presence of AuNPs is validated by the Au 4f peaks at 83.7 eV and 87.7 eV, attributed to Au $4f_{7/2}$ and Au $4f_{5/2}$, respectively,[32] suggesting the formation of AuNPs *via in situ* reduction with GluN/Alg nanocomposites. The intensity ratio of Au 4f to Fe 2p peaks increases with higher gold ion feed ratios, from 9% to 15%, indicating a rise in AuNP content in samples with higher feeding gold ion contents. Notably, the AuNPs/Fe_3O_4@GluN/Alg-9% nanocomposite exclusively contains Au(0), whereas others show both Au(0) and Au(I) oxidation states. Presence of the Au(I) is visible due to broadening of Au 4f lines in the samples with lower gold content, while in the sample with the highest gold content (15%) the shoulders due to Au(I) is clearly recognizable. This suggests that polysaccharides in samples with lower Au(0) content effectively prevent oxidation. The Au 4f surface content in nanocomposites with feeding gold ion ratios of 9%, 11%, 13%, and 15% was found to be 0.20%, 0.32%, 0.33%, and 0.41%, respectively. It proves that the gold nanoparticles are efficiently encapsulated by polysaccharide matrix. These variations significantly impact the catalytic performance of the synthesized nanocomposites.

Fig. 5 displays the XRD patterns of nanocomposite AuNPs/Fe_3O_4@GluN/Alg with varying gold ion concentrations. These patterns confirm that the nanocomposites possess a crystalline structure, with all significant peaks matching the standard patterns for Fe_3O_4 NPs (card number 04.0784) and AuNPs (card number 00-004-0783), while the organic components are amorphous. The characteristic peaks of Fe_3O_4 NPs are identifiable at 2θ positions of 30.08° (2 2 0), 35.44° (3 1 1), 37.05° (2 2 2), 43.09° (4 0 0), 53.44° (4 2 2), 57.02° (5 1 1), 62.64° (4 4 0), 67.58° (5 3 1), 71.17° (6 2 0), and 74.10° (5 3 3),[33] while the face-centered cubic (fcc) characteristics of crystalline AuNPs are observed at 2θ angles of 38.19° (1 1 1), 44.31° (2 0 0), 64.56° (2 2 0), and 77.32° (3 1 1).[34] The XRD analysis confirmed the coexistence of Fe_3O_4 NPs and AuNPs in the nanocomposites. Notably, the peak intensity at the fcc (1 1 1) plane of AuNPs

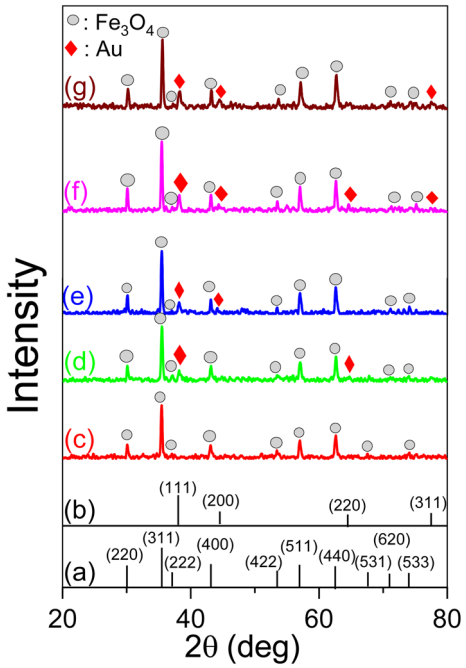

Fig. 5 Standard XRD patterns of Fe_3O_4 NPs (card number 04.0784) (a), AuNPs (card number 00-004-0783) (b) and the nanocomposites AuNPs/Fe_3O_4@GluN/Alg with different feeding ratios of gold ion: 0% (c); 9% (d); 11% (e); 13% (f); 15% (g).

increases with higher feeding gold ion ratios, indicating a rise in the crystalline AuNPs content (Table S1†). The AuNP crystal parameters in the nanocomposites were estimated using the Scherrer equation at the fcc (1 1 1) plane, revealing a crystalline size range of 17.541 to 21.86 nm. The average lattice parameter and cell volume of AuNPs were approximately 4.08 to 4.19 Å and 67.86 to 68.03 $Å^3$, respectively. Meanwhile, the Fe_3O_4 NPs crystal parameters in all the nanocomposites were calculated at the highest intensity XRD peak, namely (3 1 1). The crystallite sizes were found to be 26.90–31.39 nm. Thus, the XRD results confirmed the crystalline presence of Fe_3O_4 and AuNPs in the nanocomposite, with the crystalline size of AuNPs being suitable for catalytic reduction applications.

SEM and TEM images of the nanocomposites with different gold ion feeding ratios (0%, 9%, 11%, 13%, 15%) were analyzed to assess the impact of gold content on their morphology and particle size (Fig. 6). The SEM image of the 0% gold sample displayed uniform particles corresponding to Fe_3O_4 NPs, exceeding 100 nm in size. In contrast, nanocomposites containing AuNPs exhibited particles of varying sizes. Additionally, nanocomposites with higher feeding ratios of AuNPs showed slight morphological changes. This is likely due to the interplay between the AuNPs and polysaccharides in the samples, which influences the membrane structure of the nanocomposite at increased feeding gold contents.

TEM images revealed that the Fe_3O_4 NPs predominantly have hexagonal shapes with a monodispersed size distribution, averaging around 160 nm, which is significantly higher than the crystallite sizes from XRD data. These nanoparticles are encased in rounded organic layers attributed to the polysaccharide

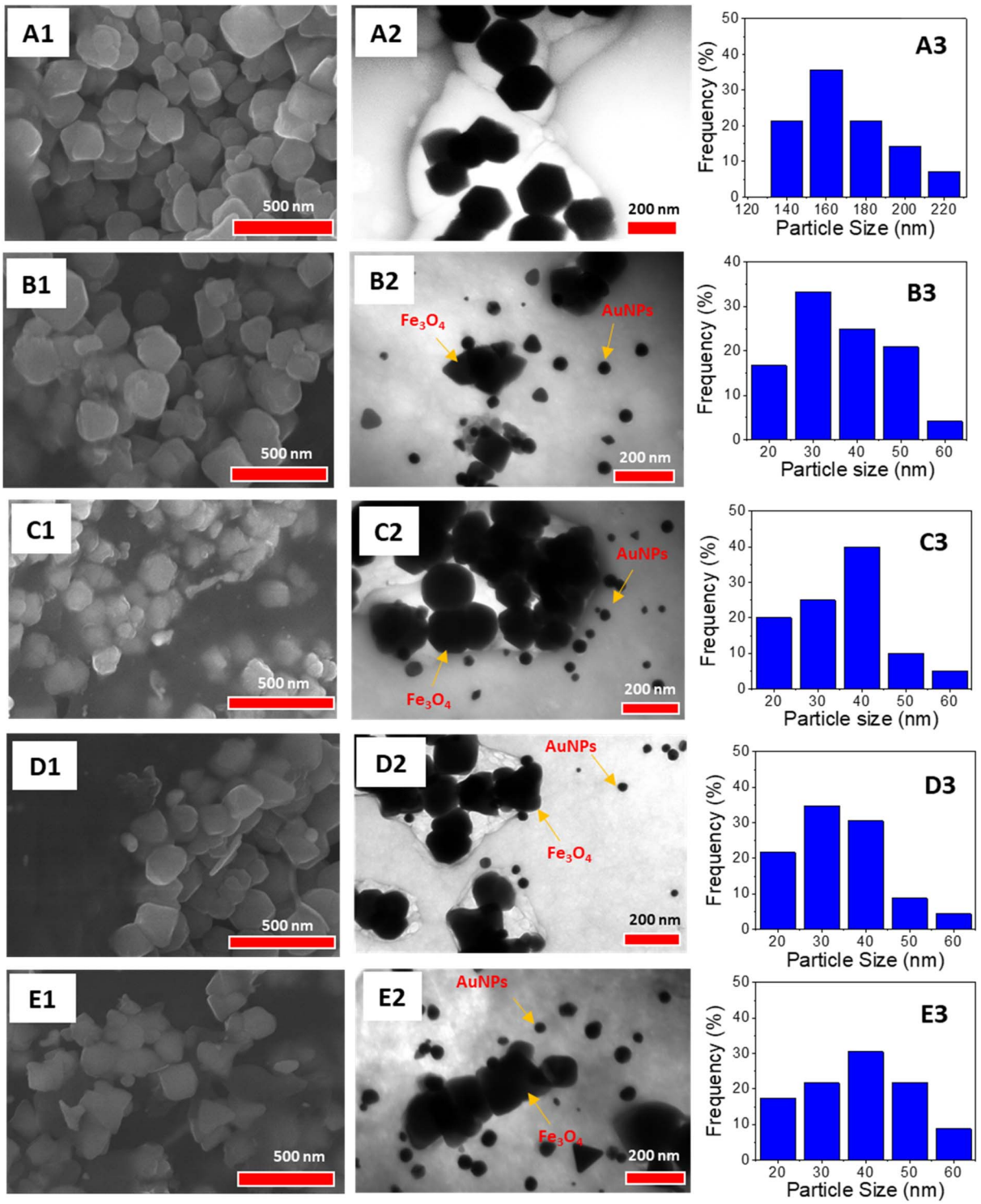

Fig. 6 SEM images (left), TEM images (center), and size distribution graphs (right) of AuNPs/Fe_3O_4@GA/Alg nanocomposites prepared with varying gold ion feed ratios: 0% (A1–A3), 9% (B1–B3), 11% (C1–C3), 13% (D1–D3), and 15% (E1–E3). For the 0% nanocomposite, the size distribution represents Fe_3O_4 nanoparticles, while for the 9–15% nanocomposites, the distribution reflects the AuNPs.

chains of GluN/Alg. *In situ* synthesis of AuNPs/Fe_3O_4@GluN/Alg showed that particle sizes slightly varied with different feeding gold ion ratios, ranging from 20 to 60 nm, which is larger than the crystalline sizes from the XRD patterns. Specifically, the nanoparticles at a 9% gold content had a highest distribution frequency around 30 nm, whereas at 15% gold content, the size increased to about 40 nm. This indicates a slight morphological change in AuNPs within the nanocomposite at different feeding ratios. Moreover, the nanocomposite AuNPs/Fe_3O_4@GluN/Alg showed minimal change in particle size of Fe_3O_4 NPs at

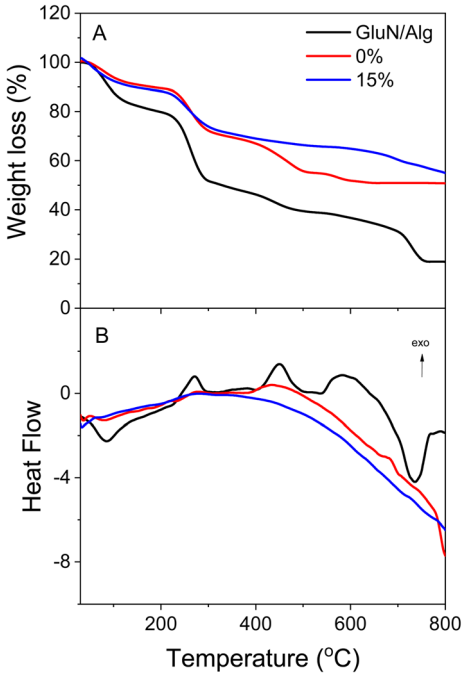

Fig. 7 TGA curves (A) and DTA curves (B) of nanogel, Fe_3O_4@GluN/Alg and AuNPs/Fe_3O_4@GluN/Alg.

different feeding ratio, confirming that the synthesis of AuNPs did not effect on morphology of Fe_3O_4 NPs (Fig. S3†).

To assess the thermal properties of the nanocomposites, TGA and DTA measurements were conducted on the GluN/Alg nanogel, magnetic nanocomposites Fe_3O_4@GluN/Alg, and AuNPs/Fe_3O_4@GluN/Alg-15% in an air flow of 20 mL min^{-1} with a heating rate of 10 °C min^{-1} (Fig. 7). The thermal behavior of the magnetic nanocomposites differed significantly from that of the GluN/Alg nanogel. The TGA curve for the nanogel indicated thermal decomposition in four stages: about 23% below 220 °C, roughly 27% between 220–300 °C, approximately 20% from 300–700 °C, and approximately 10% between 700–750 °C. In contrast, the TGA curves for Fe_3O_4@GluN/Alg and AuNPs/Fe_3O_4@GluN/Alg showed three stages: around 12% below 220 °C, about 18% from 220–300 °C, and 20% (without AuNPs) and 10% (with AuNPs) between 300–800 °C. The lower thermal decomposition of the magnetic nanocomposites below 220 °C is attributed to a low moisture content, as indicated by endothermic peaks in the DTA curves. Furthermore, the TGA data demonstrated that the inclusion of Fe_3O_4 and AuNPs significantly enhanced the thermal stability of the nanogel. The DTA curves confirmed similar thermal behavior for both magnetic nanocomposites, highlighting the crucial role of Fe_3O_4 NPs in improving the stability of the nanogel.

3.3. Recyclable catalysis reduction of nitrophenols

Nitrophenols (NiPs) are notorious organic compounds that are non-biodegradable in water, posing significant risks to both the environment and human health. This has driven the exploration of various treatment methods. Recently, the catalytic reduction of NiPs to aminophenols (AiPs) using reducing agents like $NaBH_4$ has garnered significant attention from chemists due to its environmental and pharmaceutical benefits. In the pharmaceutical industry, this catalytic reduction can yield intermediates for drug synthesis, such as paracetamol. [35–37] Among the catalysts, plasmonic metal nanoparticles (*e.g.*, AgNPs, AuNPs) have shown superior catalytic performance when paired with $NaBH_4$.

The catalytic efficacy of plasmonic metal nanoparticles (PMNPs) is significantly influenced by factors such as surface characteristics and nanometal concentration, which directly affect the binding/adsorption capability of the reactants and the release/desorption of the reaction products. In this study, we examined the catalytic activity and recyclability of AuNPs/Fe_3O_4@GluN/Alg nanocomposites with gold ion feeding ratios ranging from 0 to 15% for the reduction of 2-, 3-, and 4-NiPs. The reduction process was monitored *in situ* by measuring UV-vis absorption at ambient temperature, observing the concentration changes over time. The effectiveness of the reactions was confirmed by the discoloration of the NiP solution and a decrease in absorbance values in the UV-vis spectra. In a separate control experiment, the reduction of NiPs without a catalyst was conducted. As shown in Fig. S4,† the reduction yields without nanocatalysts were insignificant after 30 days, highlighting the crucial role of the catalyst in enhancing the reaction efficiency.

The reduction reactions were confirmed by the discoloration of NiP solutions and the recyclability of magnetic nanocatalysts using external magnetic fields, as shown in Fig. 8A–10A. The UV-vis spectra revealed a decrease in absorbance values at the relative peaks and a simultaneous increase in new peaks around 290 nm, indicating the formation of AiPs (Fig. 8–10). The results demonstrated that the reduction began immediately upon adding the nanocomposites. The reaction kinetics for all NiPs in the presence of nanocomposites were calculated using a pseudo-first-order model, with the rate constants (k_{app}) and correlation coefficients (R^2) summarized in Table S2.† The high correlation coefficients ($R^2 > 0.90$) for the reduction of all NiPs confirm that the reactions follow a pseudo-first-order kinetic model.

The completion time and reaction efficiency depend on the molecular structure of NiPs and the type of nanocomposites used. In particular, the reduction of 2-NiP was most efficient with AuNPs/Fe_3O_4@GluN/Alg, completing in about 16 minutes, whereas Fe_3O_4@GluN/Alg alone achieved only about 25% reduction in 30 minutes (Fig. 8B). Additionally, the reaction rate varied significantly with different AuNPs/Fe_3O_4@GluN/Alg nanocomposites, as shown in the UV-vis spectra. For the reaction kinetics study, the plot of $\ln(A_t/A_0)$ *versus* reaction time for 2-NiP reduction (Fig. 8G) demonstrated a linear relationship, confirming the pseudo-first-order nature of the reaction. The apparent rate constants for AuNPs/Fe_3O_4@GluN/Alg at feeding gold ion ratios of 0%, 9%, 11%, 13%, and 15% were determined from the slope of the plot, being 0.13×10^{-3} s^{-1}, 1.15×10^{-3} s^{-1}, 1.22×10^{-3} s^{-1}, 1.67×10^{-3} s^{-1}, and 2.05×10^{-3} s^{-1}, respectively (Table S1†). The highest rate constant at a 15% gold ion ratio is attributed to the high AuNPs content in the nanocomposite. In recyclability, most nanocatalysts remained stable

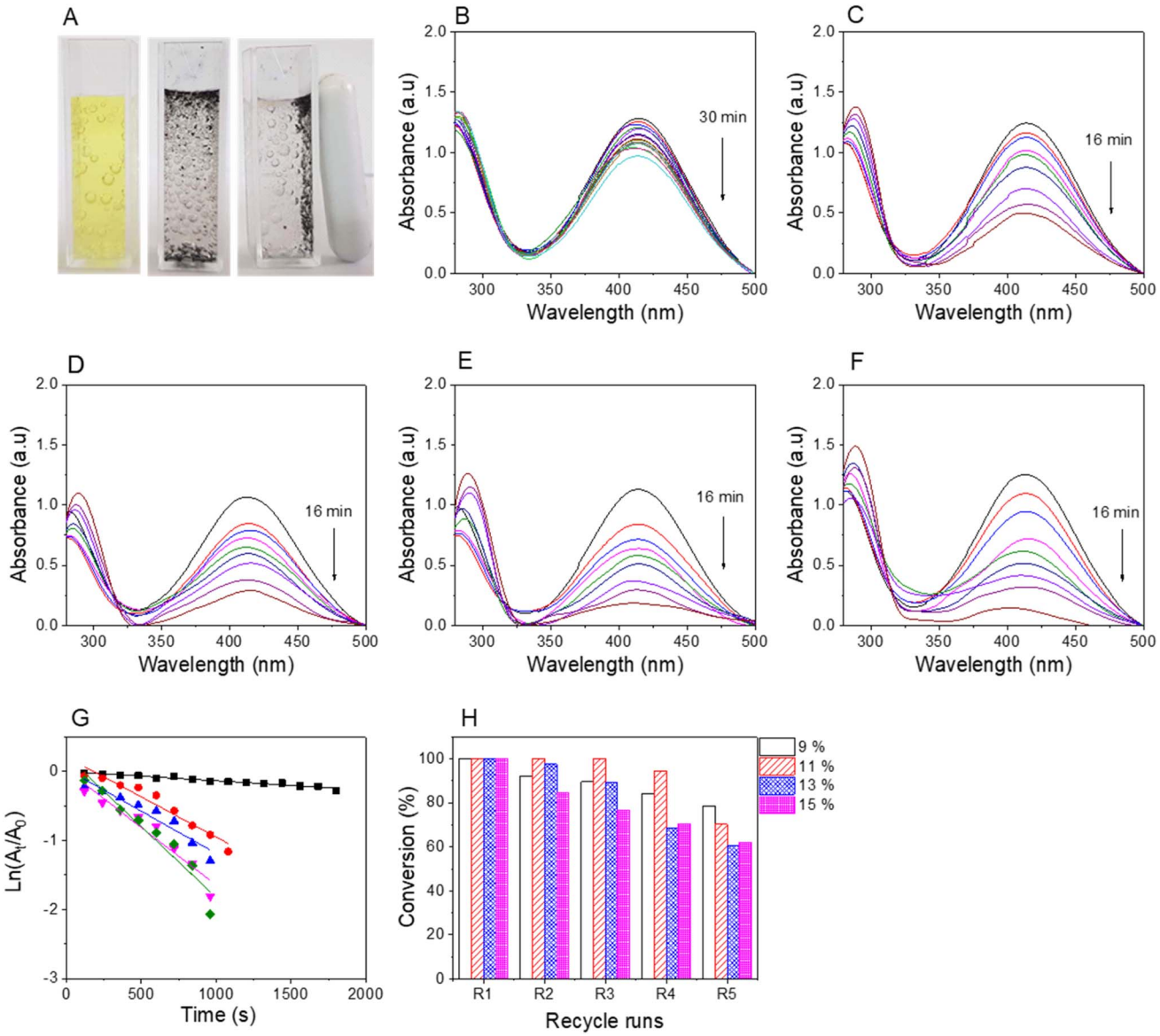

Fig. 8 Photos of 2-nitrophenol solution before and after catalytic reduction (A); UV-vis spectra for reduction of 2-nitrophenol in the presence of nanocomposite with feeding ratios of gold ions 0% (B), 9% (C), 11% (D), 13% (E), 15% (F), measured for 16 min; plots of absorbance values against reaction (G); and recyclability of the nanocomposites (H).

through the second cycle but showed a significant decrease by the fifth cycle, likely due to the loss of AuNPs during the reaction process or/and strong binding of 2-AiP to the AuNP surfaces.

The pale yellow color of the aqueous 3-nitrophenolate solution is marked by UV-vis absorption bands at 390 nm. The reduction of 3-NiP can be kinetically tracked by observing the absorbance of this peak over time. Decolorization and absorbance measurements at the peak reveal the reduction process of 3-NiP. Within 10 minutes of adding the nanocatalyst, the solutions become decolorized. The nanocatalyst can be easily collected using an external field, as demonstrated in Fig. 9A. The absorbance at 390 nm drops rapidly in the presence of AuNPs/Fe_3O_4@GluN/Alg, as shown in Fig. 9C–F, while Fe_3O_4@GluN/Alg nanocomposite results in a slower reduction rate, highlighting the critical role of AuNPs in catalyzing the reduction of 3-NiP. Kinetic analysis reveals a strong linear relationship between $\ln(A_t/A_0)$ and time (Fig. 9G). The rate constants derived from the slopes of these plots, with high correlation coefficients (R^2), are 0.11×10^{-3} s^{-1} for nanocomposite-0%, 1.35×10^{-3} s^{-1} for nanocomposite-9%, 1.57×10^{-3} s^{-1} for nanocomposite-11%, 2.02×10^{-3} s^{-1} for nanocomposite-13%, and 2.01×10^{-3} s^{-1} for nanocomposite-15% (Table S1†). It is clear that the rate constant increases with the AuNP content in the nanocomposites. Moreover, the nanocomposites demonstrate good catalytic stability after three recycling runs.

The catalytic reduction of 4-NiP using the nanocomposite indicated by a color change from yellow to colorless over time (Fig. 10A). This reduction process was confirmed through UV-vis spectra, showing a decrease in absorbance at 400 nm upon the

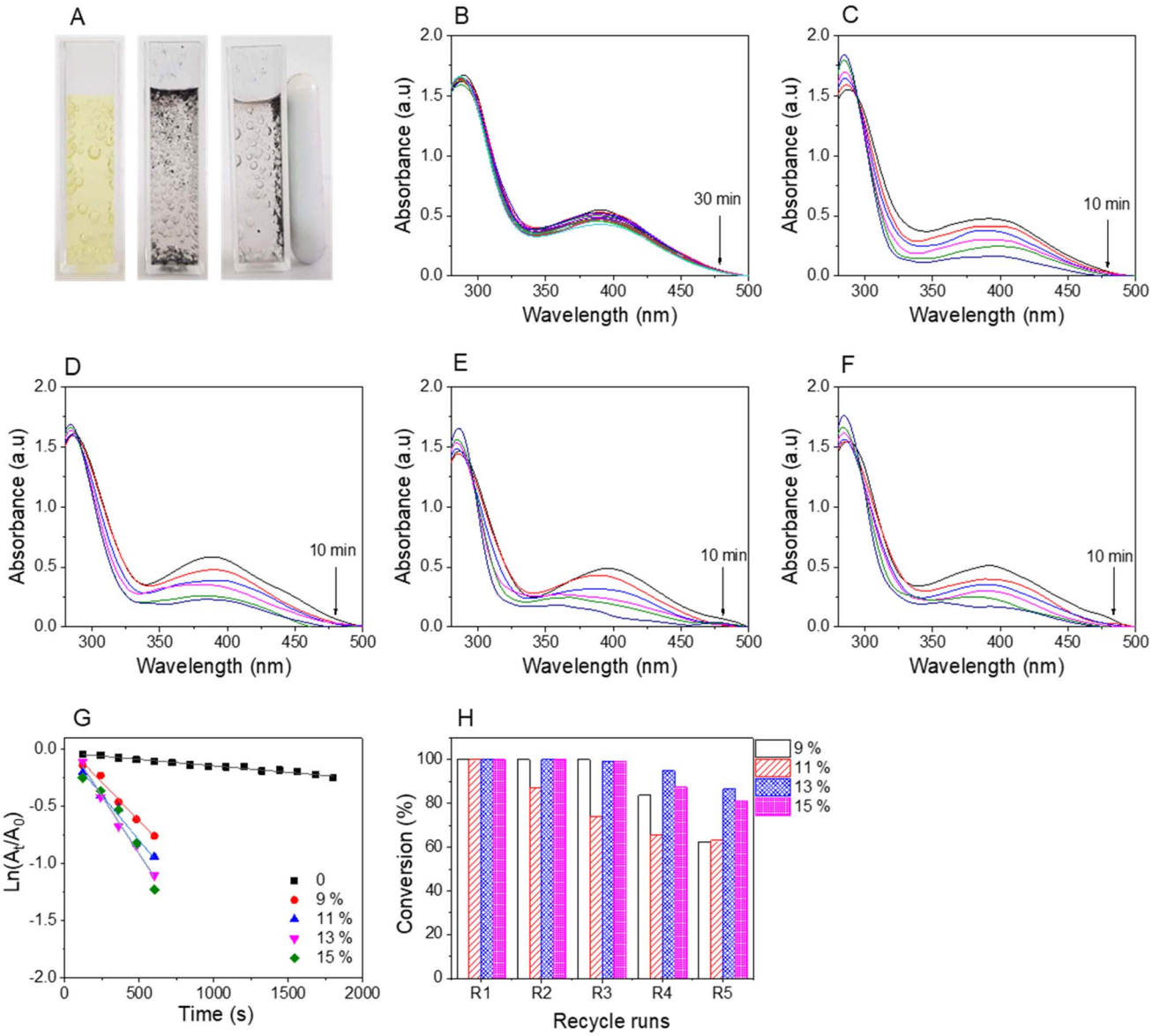

Fig. 9 Photos of 3-nitrophenol solution before and after catalytic reduction (A); UV-vis spectra for reduction of 3-nitrophenol in the presence of nanocomposite with feeding ratios of gold ions 0% (B), 9% (C), 11% (D), 13% (E), 15% (F) measured for 10 min; plots of absorbance values against reaction (G); and recyclability of the nanocomposites (H).

addition of the AuNP-based nanocomposites (Fig. 10B–F). The spectra revealed minimal reduction of 4-NiP with Fe_3O_4@GluN/Alg within 30 minutes, while significant reduction occurred within 12 minutes when AuNPs/Fe_3O_4@GluN/Alg was present. The kinetics of this reduction were analyzed by plotting absorbance at the peak *versus* time. The apparent rate constants for the nanocomposites with feeding gold ion ratios of 9%, 11%, 13%, and 15% were 1.78, 1.77, 2.02, and 2.29, respectively (Table S1†). These results indicated that the reduction rate of 4-NiP depends on the AuNP content in the nanocatalyst. Furthermore, performance stability tests of the synthesized nanocomposite demonstrated high conversion rates of over 90% across five successive reaction cycles (Fig. 10G).

Experimental findings indicate that the presence of a nanocatalyst enhances catalytic activity. The observed catalytic reduction appears to adhere to the Langmuir–Hinshelwood mechanism, wherein nanoparticles serve as adsorption sites for both dyes and BH_4^- ions. This adsorption facilitates electron transfer from BH_4^- (acting as an electron donor) to NiPs (serving as an electron acceptor), as depicted in Fig. 1. Consequently, the reaction rate is influenced by factors such as the availability of free surface area, the efficiency of adsorption and desorption, and unhindered diffusion. Additionally, the position of the $-NO_2$ group in nitrophenols (2-, 3-, or 4-NiPs) impacts their adsorption and desorption behavior on AuNPs. Notably, 2-NiP molecules exhibit slower adsorption/desorption kinetics, which likely contributes to the lower apparent rate constant for 2-NiP compared to the other isomers.

Compared to previous studies, the AuNPs/Fe_3O_4@GluN/Alg nanocomposite demonstrated superior catalytic performance

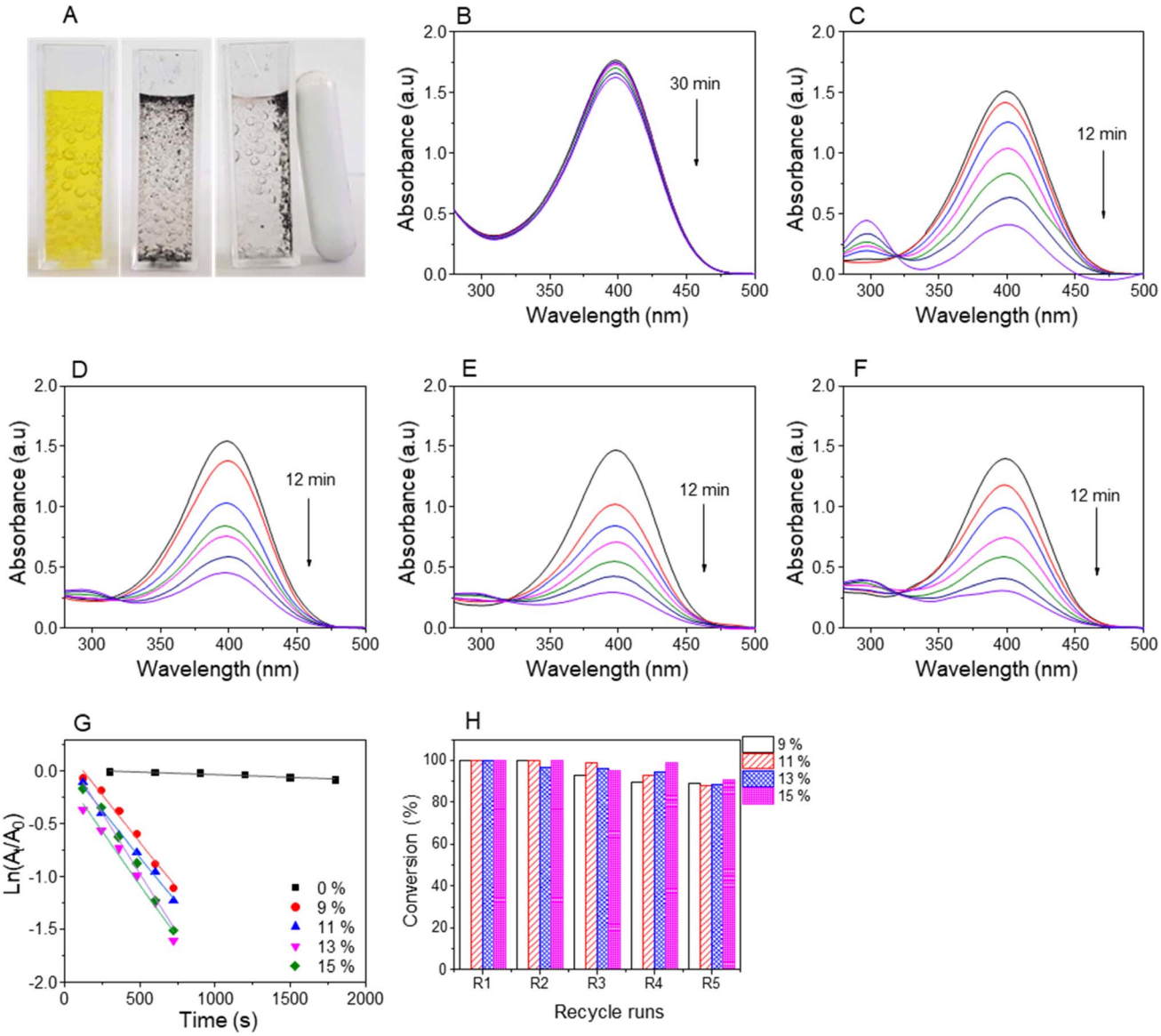

Fig. 10 Photos of 4-nitrophenol solution before and after catalytic reduction (A); UV-vis spectra of 4-nitrophenol in the presence of nanocomposite with feeding ratios of gold ions 0% (B), 9% (C), 11% (D), 13% (E), 15% (F) for measured for 12 min; plots of absorbance values against reaction (G); and recyclability of the nanocomposites (H).

Table 1 Comparison of catalytic activity of gold nanoparticles based nanocatalysts towards the reduction of nitrophenols

Dyes	Catalyst	Time (min)	k_{app} (s^{-1})	Ref.
2-NiP	TiO_2-Ag@Alg	40	0.5×10^{-3}	38
	CeO_2-SnO@Alg	9	0.57×10^{-3}	39
	AuNPs@Chitosan	20	1.3×10^{-3}	40
	AuNPs/Fe_3O_4@GluN/Alg	16	2.05×10^{-3}	This work
3-NiP	AgNPs@Gum-	10	2.2×10^{-3}	41
	AuNPs@Chitosan	10	1.4×10^{-3}	40
	AuNPs/Fe_3O_4@GluN/Alg	10	2.02×10^{-3}	This work
4-NiP	AgNPs@PVP/Alg	8	1.23×10^{-3}	42
	AgNPs@HPCD/Alg	25	1.51×10^{-3}	43
	PdNPs@HPCD/Alg	24	1.78×10^{-3}	44
	AuNPs@Chitosan	21	1.48×10^{-3}	40
	AuNPs/Fe_3O_4@GluN/Alg	12	2.29×10^{-3}	This work

over AuNP-based nanocomposites embedded into polysaccharides (Table 1). Additionally, this nanocomposite facilitated easy recycling for the reduction of nitrophenols in aqueous solutions. Consequently, the nanocomposite significantly enhanced the catalytic efficiency for nitrophenol reduction.

To assess the reuse ability, the AuNPs/Fe_3O_4@GluN/Alg nanocomposites were analyzed using TEM imaging and ICP-OES before and after five catalytic cycles of 4-NiP reduction. As shown in Fig. S5,† the morphology and size distribution of both Fe_3O_4 and AuNPs remained largely unchanged, confirming that the catalysis predominantly occurs on the AuNP surfaces. ICP-OES analysis revealed that the initial concentrations of iron and gold were 15.58 ppm and 1.20 ppm, respectively, while after five cycles, these values were 15.58 ppm and 1.01 ppm. The

observed loss of gold contributed to the reduced catalytic performance of the nanocomposite after repeated use.

Conclusions

This study introduces a novel approach for synthesizing gold nanoparticles embedded into magnetic nanocomposite of glucosamine/alginate *via* an *in situ* method. Comprehensive characterization using various analytical techniques was performed, revealing crystalline gold nanoparticles with an average diameter of 30–40 nm. The recyclable catalytic potential of the nanocomposite was then assessed for the reduction of 2-nitrophenol, 3-nitrophenol and 4-nitrophenol, utilizing $NaBH_4$. Remarkably, the reactions exhibited rapid kinetics, with pseudo-first order rate constants ranging from 1.16×10^{-3} s^{-1} to 2.29×10^{-3} s^{-1}. The nanocomposite demonstrated excellent recyclability in the reduction of 4-nitrophenol after five successful cycles with conversions above 90%. This innovative nanocomposite emerges as a promising catalyst for the reduction of nitrophenol, offering considerable potential for diverse industrial applications.

Data availability

The data supporting this article have been included as part of the ESI.†

Conflicts of interest

There are no conflicts to declare.

Acknowledgements

The authors are thankful to Vietnam Academy of Science and Technology (CSCL.15.01/22-23) for funding this work.

References

1 D. A. Giljohann, D. S. Seferos, W. L. Daniel, M. D. Massich, P. C. Patel and C. A. Mirkin, *Spherical Nucleic Acids*, 2020, pp. 55–90.
2 M. Jiang, R. H. Althomali, S. A. Ansari, E. A. M. Saleh, J. Gupta, K. D. Kambarov, H. O. Alsaab, E. R. Alwaily, B. M. Hussien, Y. F. Mustafa, A. Narmani and B. Farhood, *Int. J. Biol. Macromol.*, 2023, **251**, 126390.
3 L. Qin, G. Zeng, C. Lai, D. Huang, P. Xu, C. Zhang, M. Cheng, X. Liu, S. Liu and B. Li, *Coord. Chem. Rev.*, 2018, **359**, 1–31.
4 B. Paul and A. Tiwari, *IOSR J. Environ. Sci., Toxicol. Food Technol.*, 2015, **1**(4), 1–7.
5 G. Li and R. Jin, *Nanotechnol. Rev.*, 2013, **2**(5), 529–545.
6 D. Astruc, Introduction: nanoparticles in catalysis, *Chem. Rev.*, 2020, **120**, 461–463.
7 P. B. Santhosh, J. Genova and H. Chamati, *Chemistry*, 2022, **4**(2), 345–369.
8 K. Kalimuthu, B. S. Cha, S. Kim and K. S. Park, *Microchem. J.*, 2020, **152**, 104296.
9 C. Liang, J. Y. Cheong, G. Sitaru, S. Rosenfeldt, A. S. Schenk, S. Gekle, I. D. Kim and A. Greiner, *Adv. Mater. Interfaces*, 2022, **9**(4), 2100867.
10 T. Ishida, T. Murayama, A. Taketoshi and M. Haruta, *Chem. Rev.*, 2019, **120**(2), 464–525.
11 M. Kazemi, *Synth. Commun.*, 2020, **50**(14), 2079–2094.
12 T. Zeng, H.-y. Niu, Y.-r. Ma, W.-h. Li and Y.-q. Cai, *Appl. Catal., B*, 2013, **134**, 26–33.
13 R. Ahmad, N. Griffete, A. Lamouri, N. Felidj, M. M. Chehimi and C. Mangeney, *Chem. Mater.*, 2015, **27**(16), 5464–5478.
14 M. Falahati, F. Attar, M. Sharifi, A. A. Saboury, A. Salihi, F. M. Aziz, I. Kostova, C. Burda, P. Priecel and J. A. Lopez-Sanchez, *Biochim. Biophys. Acta*, 2020, **1864**(1), 129435.
15 D. P Facchi, J. A da Cruz, E. G Bonafe, A. GB Pereira, A. R Fajardo, S. AS Venter, J. P Monteiro, E. C Muniz and A. F Martins, *Curr. Med. Chem.*, 2017, **24**(25), 2701–2735.
16 H. Liu, M. Zhang, F. Meng, A. Wubuli, S. Li, S. Xiao, L. Gu and J. Li, *Int. J. Biol. Macromol.*, 2024, **265**, 130824.
17 X. Liu, X. Yang, H. Xin, X. Tang, L. Weng, Y. Han and D. Geng, *Dig. J. Nanomater. Biostructures*, 2016, **11**(2), 337–348.
18 S. S. Pati, L. H. Singh, E. Guimarães, J. Mantilla, J. Coaquira, A. Oliveira, V. K. Sharma and V. K. Garg, *J. Alloys Compd.*, 2016, **684**, 68–74.
19 S. Kang, A. Rahman, E. Boeding and P. J. Vikesland, *Analyst*, 2020, **145**(12), 4358–4368.
20 S. Saha, A. Pal, S. Kundu, S. Basu and T. Pal, *Langmuir*, 2010, **26**(4), 2885–2893.
21 Y. Li, G. Li, W. Li, F. Yang and H. Liu, *Nano*, 2015, **10**(08), 1550108.
22 R. Ghorbani-Vaghei, H. Veisi, M. H. Aliani, P. Mohammadi and B. Karmakar, *J. Mol. Liq.*, 2021, **327**, 114868.
23 N. T. T. Tu, T. L.-A. Vo, T. T.-T. Ho, K.-P. T. Dang, V.-D. Le, P. N. Minh, C.-H. Dang, V.-T. Tran, V.-S. Dang and T. T. K. Chi, *Beilstein J. Nanotechnol.*, 2023, **14**(1), 781–792.
24 T. T.-T. Ho, C.-H. Dang, T. K.-C. Huynh, T. K.-D. Hoang and T.-D. Nguyen, *Carbohydr. Polym.*, 2021, **251**, 116998.
25 P. Gadziński, A. Froelich, B. Jadach, M. Wojtyłko, A. Tatarek, A. Białek, J. Krysztofiak, M. Gackowski, F. Otto and T. Osmałek, *Pharmaceutics*, 2023, **15**(1), 108.
26 M. M. Gonçalves, D. F. Maluf, R. Pontarolo, C. K. Saul, E. Almouazen and Y. Chevalier, *Int. J. Pharm.*, 2023, **642**, 123164.
27 T.-D. Nguyen, T. Hong-Ngan Tran, C.-H. Nguyen, C. Im and C.-H. Dang, *Chemical and Biochemical Engineering Quarterly*, 2015, 29, 3, pp. 429–435.
28 T. V. Thien, T.-T. Vo, V.-D. Le, C.-H. Dang, V.-S. Dang, N. T. H. Le, T. T. K. Chi, N. T. T. Tu, H. Vu-Quang and T.-D. Nguyen, *J. Organomet. Chem.*, 2024, 123161.
29 V. C. N. Anh, D. T. N. Hoa, N. T. Son, N. T. T. Uyen, N. N. U. Thu, T. N. Tuyen and D. Q. Khieu, *Beilstein J. Nanotechnol.*, 2024, **15**(1), 475–489.
30 W. Liu, D. Sun, J. Fu, R. Yuan and Z. Li, *RSC Adv.*, 2014, **4**(21), 11003–11011.
31 F. Han, L. Ma, Q. Sun, C. Lei and A. Lu, *Nano Res.*, 2014, **7**, 1706–1717.

32 L. Zhao, Y. Wang, X. Zhao, Y. Deng, Q. Li and Y. Xia, *Nanomaterials*, 2018, **8**(7), 507.
33 V. Silva, P. Andrade, M. Silva, L. D. L. S. Valladares and J. A. Aguiar, *J. Magn. Magn. Mater.*, 2013, **343**, 138–143.
34 A. K. Singh and O. Srivastava, *Nanoscale Res. Lett.*, 2015, **10**, 1–12.
35 Y. Li, Y. Ma, Y. Zhang, X. Wang and F. Bai, *Arabian J. Chem.*, 2020, **13**(12), 8613–8625.
36 R. R. Steendam, L. Keshavarz, B. de Souza and P. J. Frawley, *J. Chem. Thermodyn.*, 2019, **133**, 85–92.
37 R. Joncour, N. Duguet, E. Métay, A. Ferreira and M. Lemaire, *Green Chem.*, 2014, **16**(6), 2997–3002.
38 F. I. A. E. Fadl and M. F. A. Taleb, *J. Inorg. Organomet. Polym. Mater.*, 2023, **33**, 2142–2153.
39 E. M. Bakhsh, K. Akhtar, T. M. Fagieh, A. M. Asiri and S. B. Khan, *Int. J. Biol. Macromol.*, 2021, **191**, 243–254.
40 Q. Zhu, W. Zhang, J. Cai, J. Li, L. Zhong, S. Pu and A. Li, *Colloids Surf., A*, 2022, **640**, 128471.
41 R. Vadakkekara, M. Chakraborty and P. Parikh, *Colloid J.*, 2014, **76**, 12–18.
42 Y. Gao, X. Ding, Z. Zheng, X. Cheng and Y. Peng, *Chem. Commun.*, 2007, (36), 3720–3722.
43 T.-D. Nguyen, C.-H. Dang and D.-T. Mai, *Carbohydr. Polym.*, 2018, **197**, 29–37.
44 T.-D. Nguyen, T.-T. Vo, C.-H. Nguyen, V.-D. Doan and C.-H. Dang, *J. Mol. Liq.*, 2019, **276**, 927–935.